ADVANCED MATERIALS INTERFACES

Supporting Information

for *Adv. Mater. Interfaces,* DOI: 10.1002/admi.202102035

ALD-Coated Mesoporous Iridium-Titanium Mixed Oxides: Maximizing Iridium Utilization for an Outstanding OER Performance

Marvin Frisch, Muhammad Hamid Raza, Meng-Yang Ye, René Sachse, Benjamin Paul, René Gunder, Nicola Pinna, and Ralph Kraehnert**

Supporting Information

ALD-coated Mesoporous Iridium-Titanium Mixed Oxides: Maximizing Iridium Utilization for an Outstanding OER Performance

Marvin Frisch‡, Muhammad Hamid Raza‡, Meng-Yang Ye, René Sachse, Benjamin Paul, René Gunder, Nicola Pinna and Ralph Kraehnert**

Table of Contents

Section-I: Morphological analysis of mp. TiO_2 prior to and after ALD *via* SEM

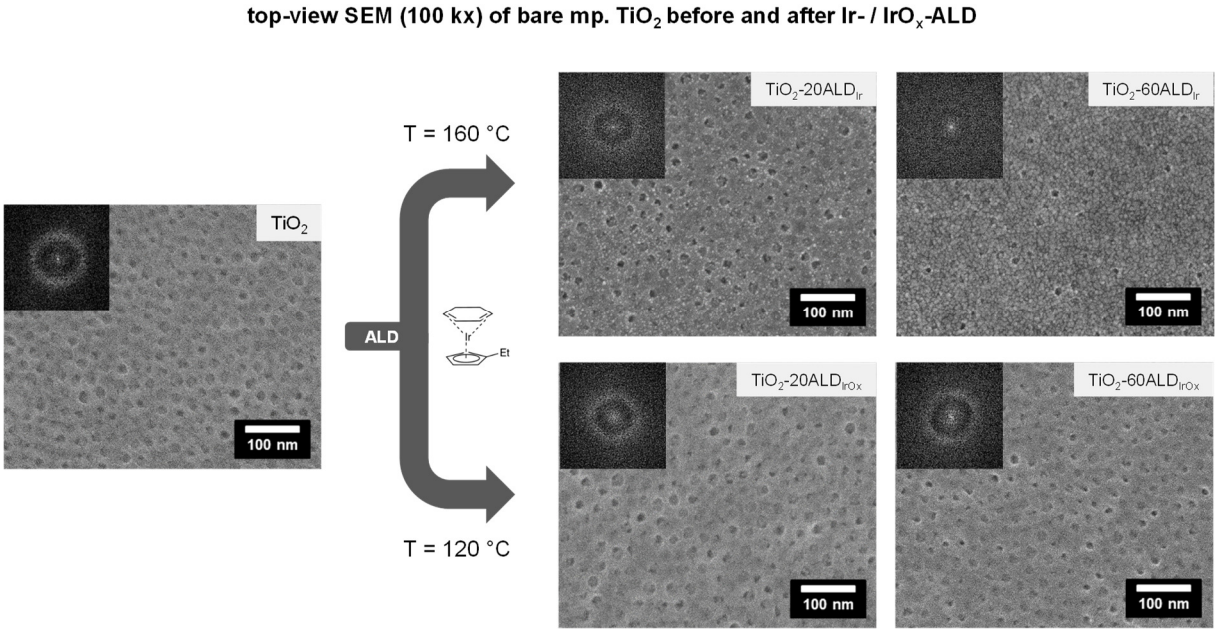

Figure S1. Representative top-view SEM images (100,000x magnification) of mp. TiO_2 films prior to ALD (left) and after ALD at different temperatures (top right: ALD at 160 °C, bottom right: ALD at 120 °C). The images were acquired for films deposited on Si substrates. Corresponding FFT images are shown as insets for each of the top-view SEM images.

Figure S1 illustrates the results from SEM analysis of unmodified, weakly conductive TiO_2 support films prior to ALD (left). The corresponding FFT reveals the formation of a locally ordered mesoporosity after calcination for 20 min at 475 °C in air and a concomitant removal of the polymer template. After 20 ALD cycles at 160 °C, bright spots appear at the surface of the films which indicate the presence of nanoparticulate Ir-rich species. After 60 cycles ALD at 160 °C, these nanoparticles have grown in size and cover almost the entire surface of the film. The mesoporous structure is hence only partially preserved. This is further corroborated by the corresponding FFT inset of TiO_2-60ALD_{Ir}. Contrarily, ALD at 120 °C ensures the deposition of layer-like surface deposits over the range of investigated ALD cycle numbers.

Overall, the results are in good agreement with the observations from the morphological analysis of the mp. $IrTiO_x$ supports presented in **Figure 1** in the main part of this work.

Section-II: Lower magnification SEM of mp. TiO_2 and mp. $IrTiO_x$ prior to and after ALD

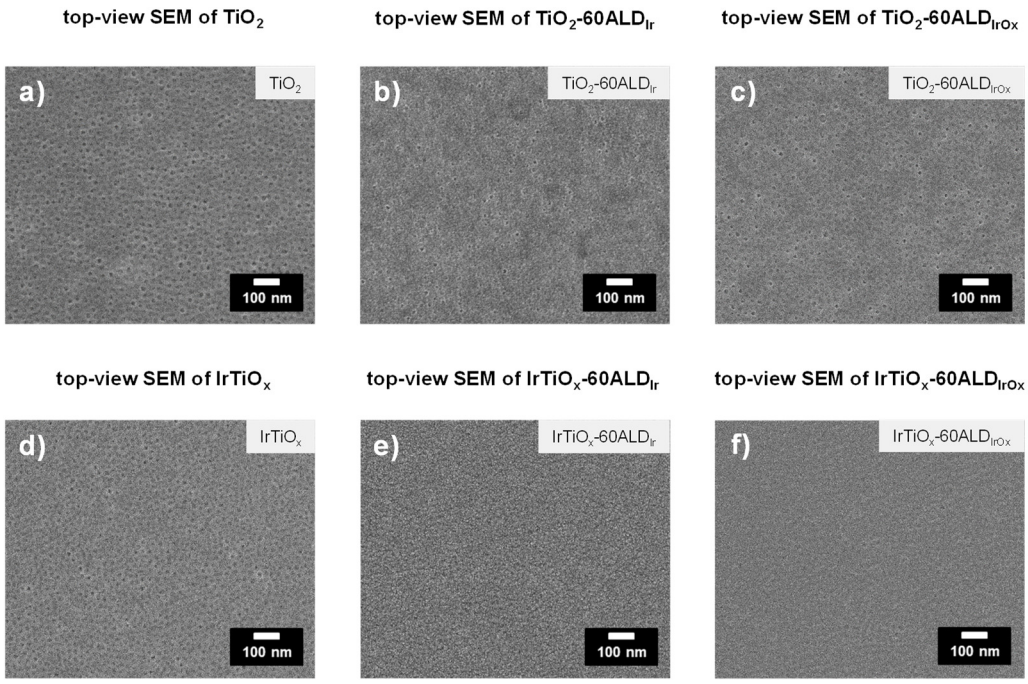

Figure S2. Lower magnification top-view SEM images of mp. TiO_2 (a) prior to ALD, (b) after 60 cycles of Ir-ALD at 160 °C and (c) after 60 cycles of IrO_x-ALD at 120 °C. In (d) – (f), the corresponding images for mp. $IrTiO_x$ prior to and after Ir-/IrO_x-ALD are shown. All images were acquired for films deposited on Si substrates.

Figure S2 shows representative SEM images in a lower magnification of 50,000x for both mp. TiO_2 and mp. $IrTiO_x$ support films prior to ALD (a,d) and after ALD at 160 °C (b,e) as well as after ALD at 120 °C (c,f). The acquired SEM images suggest the predominance of well-defined, crack-free mesoporous structures for all coatings, independent of ALD temperature and cycle number.

Section-III: Structural and phase analysis of mp. TiO_2 prior to and after ALD *via* TEM and SAED

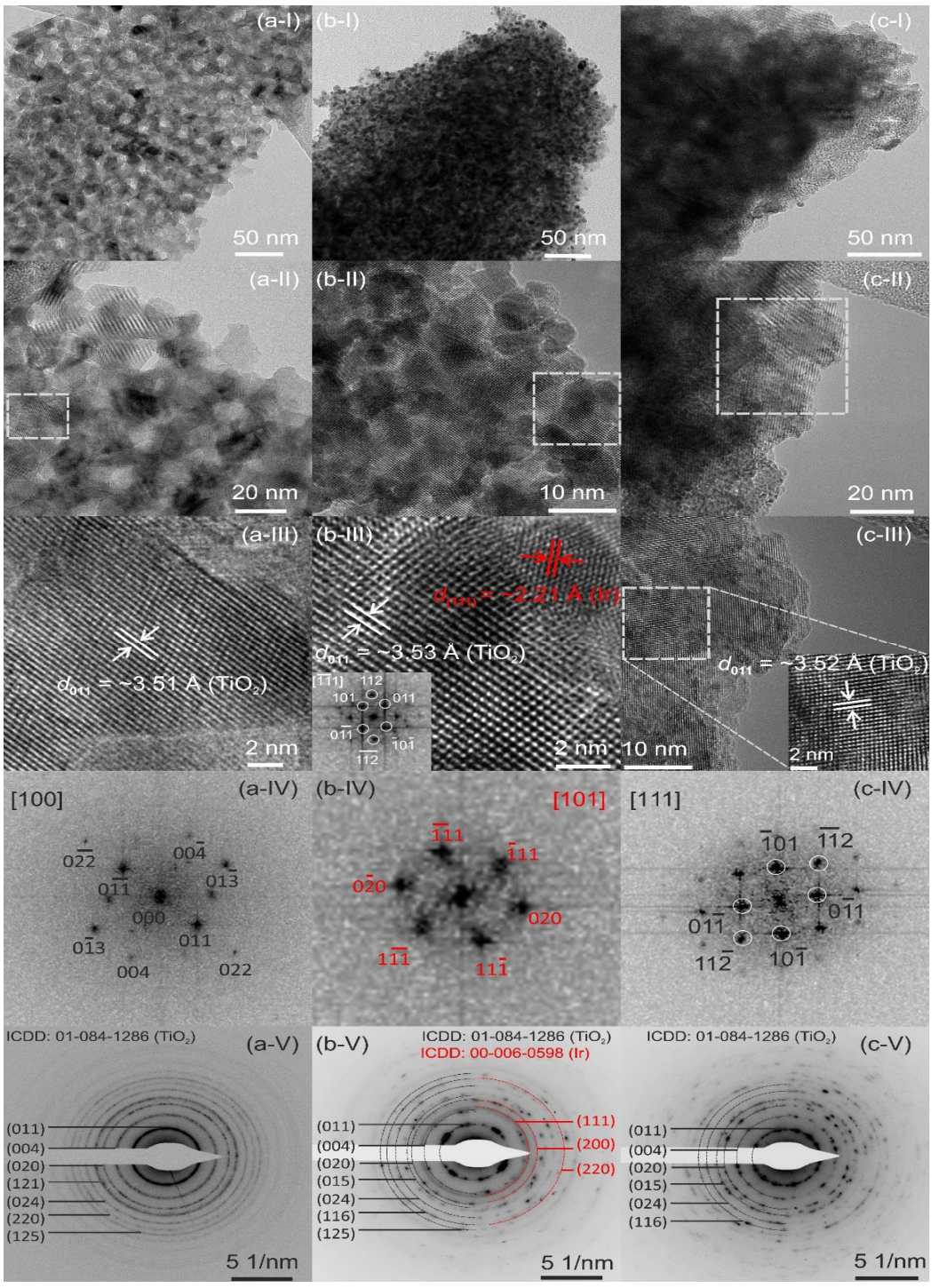

Figure S3. BF-HRTEM images (I-III), power spectra (IV) of the selected regions and SAED patterns (V) for (a) mp. TiO_2, (b) after 60 cycles ALD at 160 °C (TiO_2-60ALD_{Ir}) and (c) after 60 cycles ALD at 120 °C (TiO_2-60ALD_{IrOx}). Patterns are assigned according to the reference ICDD card numbers 01-084-1286 and 00-006-0598 for TiO_2 (anatase) and Ir^0 (cubic), respectively. Red color highlights features corresponding to Ir^0.

The lattice fringes and the PS corresponding to the selected region in the HRTEM image in **Figure S3a, II** are typical for the anatase phase of TiO_2 (**Figure S3a, III-IV**). In addition, the concentric rings in the SAED pattern show reflections corresponding to the anatase planes for TiO_2 (**Figure S3a, V**). This shows that mp. TiO_2 is composed of a nanocrystalline anatase phase after calcination for 20 min at 475 °C in air.

After 60 ALD cycles at 160 °C, the lattice fringes in the HRTEM image and the corresponding PS of the selected areas in **Figure S3b-c, II** clearly reveal the presence of two distinct regions of TiO_2 (marked with white color and the corresponding PS as an inset in **Figure S3b, III**) alongside metallic Ir^0 (highlighted with red color and the corresponding PS in **Figure S3b, IV**), where the interface between the mp. TiO_2 and the ALD-deposited Ir species can be identified as shown in **Figure 3b, III**.

Notably, after 60 ALD cycles at 120 °C, no distinct signals for any metallic Ir^0 surface species introduced *via* ALD can be found (**Figure S3c, II-V**). In fact, weak signals corresponding to IrO_2 (rutile) can be identified in the SAED pattern of ALD-coated $IrTiO_x$ at 120 °C (**Figure S3c, V**).

Section-IV: Elemental mappings of mp. $IrTiO_x$ and mp. TiO_2 films prior to and after ALD

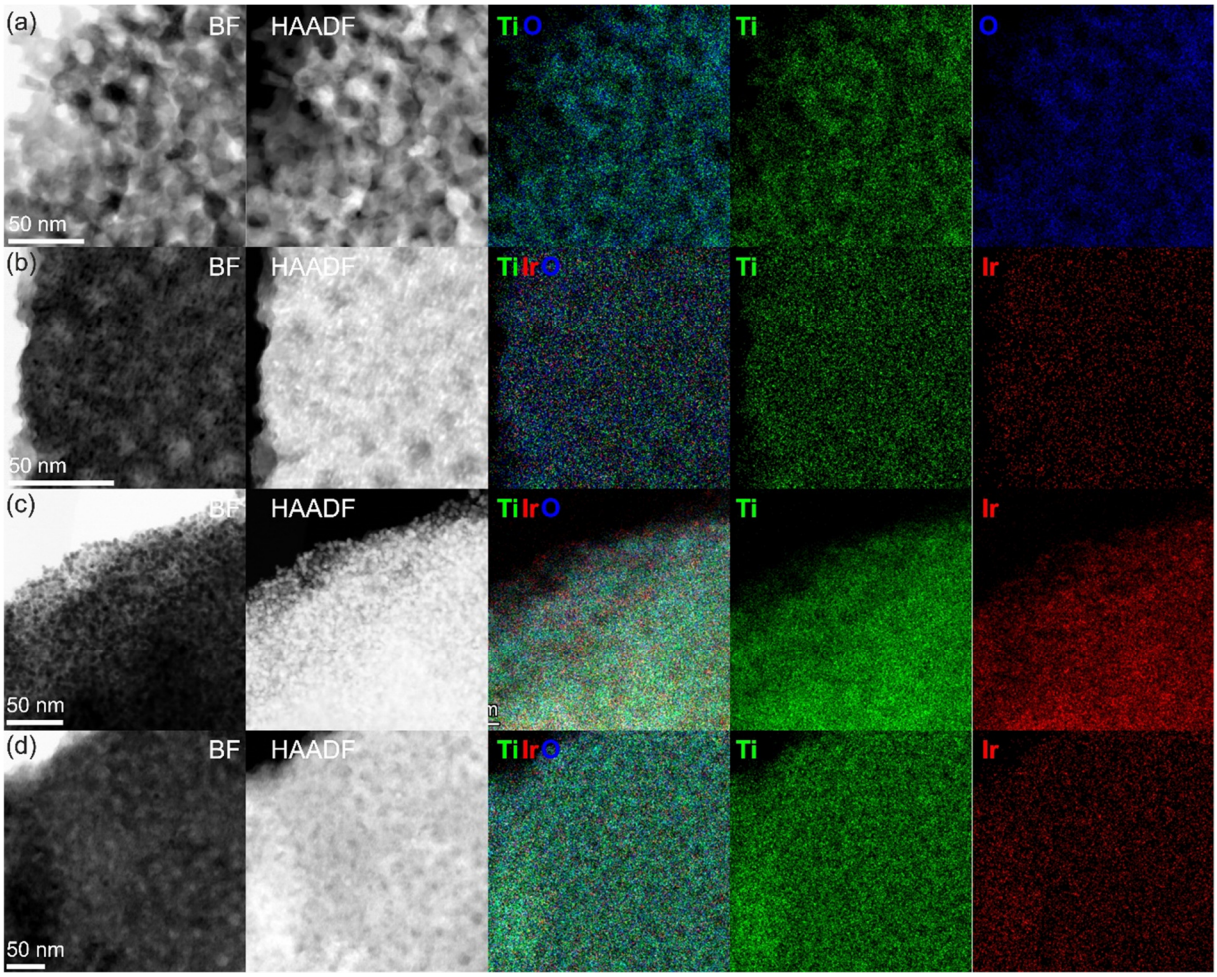

Figure S4-I. BF-STEM, HAADF-STEM images and corresponding EDX mappings for (a) mp. TiO_2 and (b) mp. $IrTiO_x$ prior to ALD, as well as for (c) TiO_2-$60ALD_{Ir}$ and (d) TiO_2-$60ALD_{IrOx}$ after 60 cycles ALD at 160 °C and at 120 °C, respectively.

The BF-STEM images of both TiO_2 and $IrTiO_x$ support films reveal a similar homogeneous mesoporous structure prior to ALD. Regarding the $IrTiO_x$ support, the corresponding elemental mapping underlines a uniform distribution of the Ir species throughout the pore walls.

For the sake of better visibility, the impact of the ALD process and temperature was examined using Ir-free TiO_2 films as support materials. BF-STEM images (c) and (d) clearly indicate the preserved mesoporosity after both ALD processes at 160 °C and at 120 °C. Moreover, the elemental mappings confirm a homogeneous distribution of ALD-introduced Ir / IrO_x species.

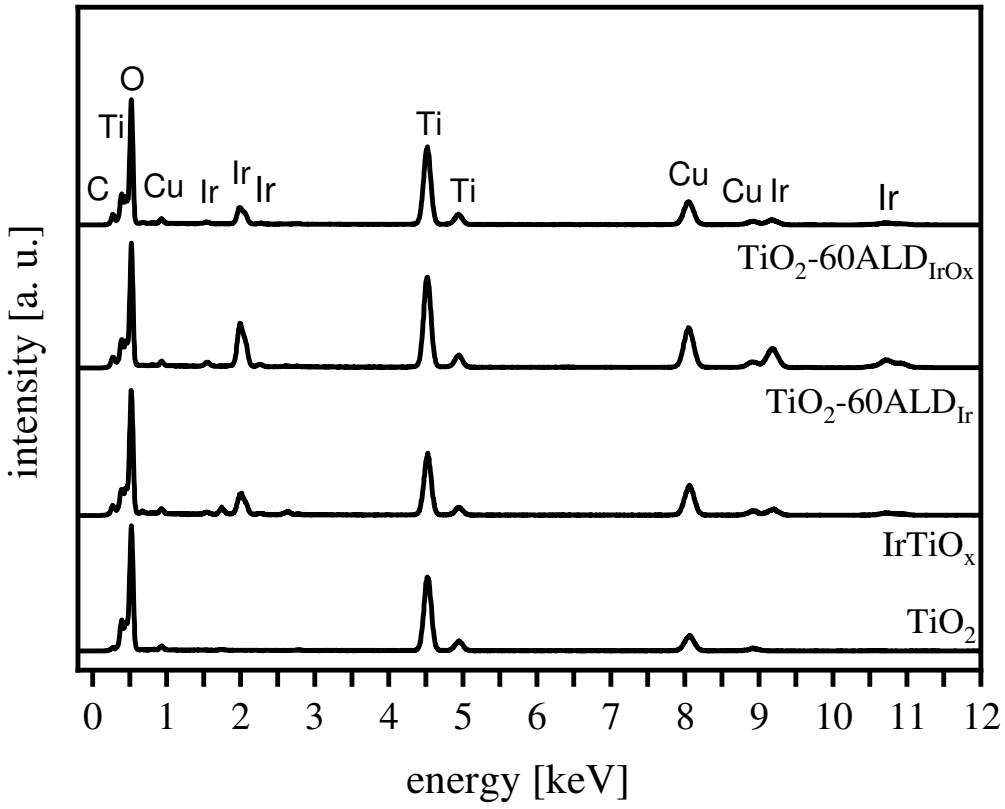

Figure S4-II. TEM-EDX spectra of mp. $IrTiO_x$ (grey) and mp. TiO_2 (black) corresponding to the EDX elemental mapping illustrated in **Figure S4-I**.

Section-V: XPS analysis of fresh and spent mp. $IrTiO_x$ and mp. TiO_2 films prior to and after ALD at 160 °C

In order to study the composition and chemical states of the surface atoms prior to and after ALD at 160 °C, XPS spectra were collected and illustrated in the following (**Figure S5**). Fresh and spent catalyst films on Ti substrates were analyzed to track the influence of OER in acidic electrolyte onto the nature of the surface Ir species. Due to the better signal-to-noise ratio as a consequence of a higher amount of Ir at the surface, the results for supports modified with 60 ALD cycles will be discussed here. In this context, it has to be noted that similar trends regarding the impact of the oxidative conditions during OER catalysis in acidic electrolyte were observed for the 20 cycle modified support films.

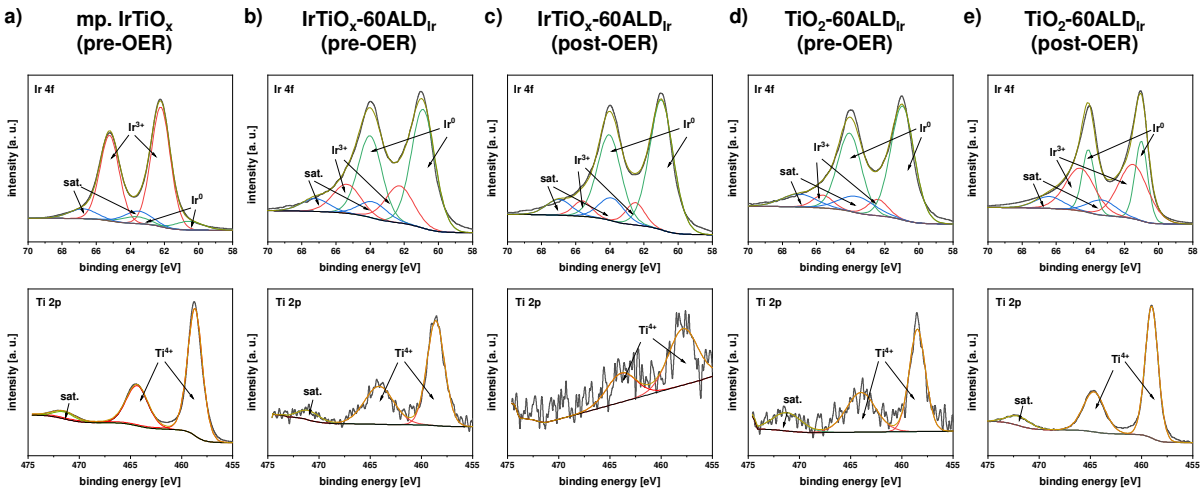

Figure S5. XPS spectra for (a) mp. $IrTiO_x$, (b) $IrTiO_x$-$60ALD_{Ir}$ prior to catalytic testing and (c) $IrTiO_x$-$60ALD_{Ir}$ post-OER in 0.5 M H_2SO_4 as well as (d) TiO_2-$60ALD_{Ir}$ prior to catalytic testing and (e) TiO_2-$60ALD_{Ir}$ post-OER in 0.5 M H_2SO_4. The upper row shows the corresponding Ir 4f spectra with deconvolution of the data and the lower row shows the Ti 2p spectra. All spectra were acquired for films deposited on Ti substrates.

Prior to ALD, the Ir 4f spectrum of mp. $IrTiO_x$ (see **Figure S5a, top**) shows a prominent doublet peak at 62.2 eV corresponding to Ir^{3+} with a characteristic doublet separation of ~ 3.0 eV and broad satellite features corresponding to Ir^{3+}.[1,2] A minor contribution of metallic Ir^0 surface species can be found. As given in **Table S1**, the relative fraction of Ir^{3+} is ten-fold higher than that of Ir^0.

After ALD at 160 °C, however, the most prominent feature can be found at lower binding energies, indicating predominantly Ir^0 species at the surface, since a doublet at 61.0 eV arises for $IrTiO_x$-60ALD_{Ir} (**Figure S5b, top**).[1,2] This is in good agreement with the results from TEM and SAED analyses revealing presence of metallic Ir^0 species for $IrTiO_x$-60ALD_{Ir} (see **Figure 3b** in the main part). Strikingly, after 150 CVs in acidic electrolyte, $IrTiO_x$-60ALD_{Ir} shows a similar surface composition compared to the fresh catalyst (**Figure S5c**). The ALD-deposited nanocrystalline Ir species did not undergo significant oxidation during OER in acid, accordingly. The ratio of Ir^0/Ir^{3+} (**Table S1**) remained similar with 6.3/1 for the fresh $IrTiO_x$-60ALD_{Ir} catalyst and only slightly increased to 6.6/1 for the spent $IrTiO_x$-60ALD_{Ir} catalyst after OER.

For Ir-ALD-modified TiO_2, predominantly metallic Ir^0 surface species can be found according to the XPS data in **Figure S5d**. Analysis of the spent catalyst film after OER, however, indicated a partial conversion of Ir^0 sites to Ir^{3+} after repeated cycling up to a potential of 1.65 V_{RHE}. The ratio drops from 8.3/1 for the fresh TiO_2-60ALD_{Ir} catalyst to 1.6/1 for the spent TiO_2-60ALD_{Ir} film (see **Table S1**). An oxidation of Ir^0 species to Ir species with higher oxidation states has been previously reported in literature[3].

Table S1. Elemental composition at the surface of the catalyst films analyzed *via* XPS prior to and after Ir-ALD at 160 °C as well as prior to and after OER catalytic testings in 0.5 M H_2SO_4.

catalyst	**ratio of Ir^0 / Ir^{3+}**
$IrTiO_x$	0.1 / 1
$IrTiO_x$-60ALD_{Ir} (pre-OER)	6.3 / 1
$IrTiO_x$-60ALD_{Ir} (post-OER)	6.6 / 1
TiO_2-60ALD_{Ir} (pre-OER)	8.3 / 1
TiO_2-60ALD_{Ir} (post-OER)	1.6 / 1

Section-VI: XPS analysis of mp. $IrTiO_x$ and mp. TiO_2 films prior to and after ALD at 120 °C

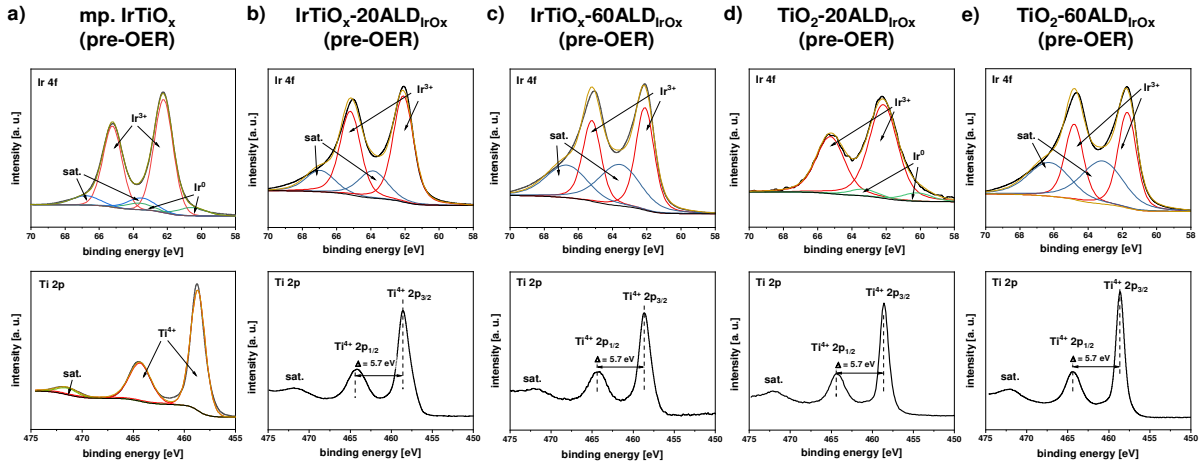

Figure S6. XPS spectra for (a) mp. $IrTiO_x$, (b) $IrTiO_x$-$20ALD_{IrOx}$, (c) $IrTiO_x$-$60ALD_{IrOx}$, (d) TiO_2-$20ALD_{IrOx}$ and (e) TiO_2-$60ALD_{IrOx}$ prior to catalytic OER testing. The upper row illustrates the corresponding Ir 4f spectra with deconvolutions of the acquired data and the lower row shows the Ti 2p spectra. All spectra were acquired for films deposited on Si substrates.

To examine the impact of temperature during the ALD process on the oxidation state of the deposited Ir species, further XPS analyses were performed for low-temperature ALD-modified films. The obtained Ir 4f and Ti 2p spectra are illustrated in Figure S6. In general, all ALD-modified films show a doublet peak at 62.2 eV with broad satellite features centered at 63.5 eV, corresponding to Ir^{3+}.[1,2,4,5] The assignment of Ir^{3+} corresponding to amorphous IrO_x was previously described by a model of IrO_6 octahedra located in the near-surface region of the IrO_x framework. The creation of an Ir vacancy leads to a change in the oxidation state of the surrounding oxygen atoms from –II to the formal oxidation state of -I. This oxidation process produces two additional electrons which are distributed among neighboring Ir^{4+} sites reducing them to Ir^{3+}.[6]

Regarding the surface Ti species, all films show a characteristic signal for Ti^{4+}, *i.e.* a doublet peak at 458.6 eV with a broad satellite feature centered at ~ 472 eV. The distance between the $2p_{1/2}$ and the $2p_{3/2}$ peak lies in the typical range of Δ = 5.7 eV.[7] The O 1s spectra (data not shown) are similar for all films and show three different kinds of contributions. The major

contribution at 530.0 eV corresponds to a Ti-O interaction. Two additional peaks at 531.5 eV and at 532.8 eV, which can be assigned to C=O species and surface –OH groups, respectively, were found. These features are typical for ALD-coated metal oxide surfaces.[7,8] Table S2 provides an overview of the ratio of surface Ti to surface Ir species prior to and after ALD at 120 °C. With an increasing number of ALD cycles, a lower ratio of Ti / Ir is found for both types of supports. This indicates an increasing coverage of the pore wall surface with ALD-deposited IrO_x species of predominantly +III oxidation state.

Table S2. Elemental composition at the surface of the catalyst films analyzed *via* XPS prior to and after IrO_x-ALD at 120 °C.

catalyst	**ratio of Ti / Ir**
$IrTiO_x$	1 / 0.3
$IrTiO_x$-20ALD_{IrOx}	1 / 1.5
$IrTiO_x$-60ALD_{IrOx}	1 / 5.3
TiO_2-20ALD_{IrOx}	1 / 0.7
TiO_2-60ALD_{IrOx}	1 / 1.8

Section-VII: GI-XRD analysis of mp. $IrTiO_x$ and mp. TiO_2 films prior to and after ALD at 120 °C and 160 °C

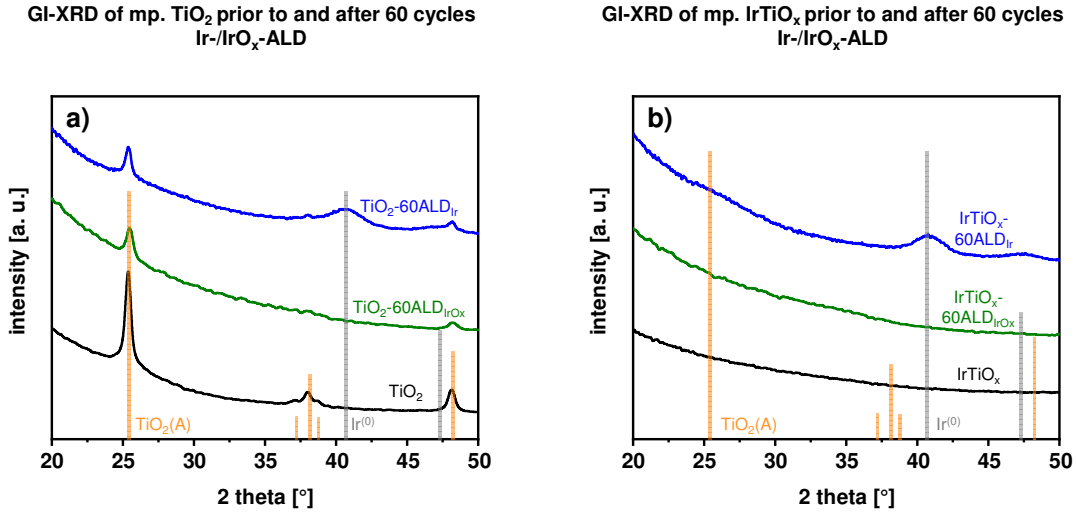

Figure S7. GI-XRD patterns of mp. TiO_2 (a) and mp. $IrTiO_x$ (b) prior to (black) and after 60 cycles ALD at 120 °C (green) and at 160 °C (blue). Reference patterns for anatase-TiO_2 (orange vertical bars) and metallic Ir (grey vertical bars) are given in (a) & (b). The results indicate the formation of a nanocrystalline TiO_2 film with anatase crystal structure (a) and an amorphous material for $IrTiO_x$ prior to ALD (b). After ALD at 160 °C, reflections for metallic Ir species appear for both TiO_2-$60ALD_{Ir}$ and $IrTiO_x$-$60ALD_{Ir}$. After ALD at 120 °C, however, no additional reflections can be found.

Notably, after 60 cycles of ALD at 120 °C, no distinct signals for any metallic Ir^0 surface species introduced *via* ALD can be found (**Figure S7a-b, green graphs**). In addition to the SEM images shown in **Figure 1**, this is another proof for the deposition of thin, layer-like structures *via* ALD at 120 °C, which do not provide sufficient scattering intensities.

Section-VIII: Electrical sheet conductivities of mp. TiO_2 prior to and after ALD

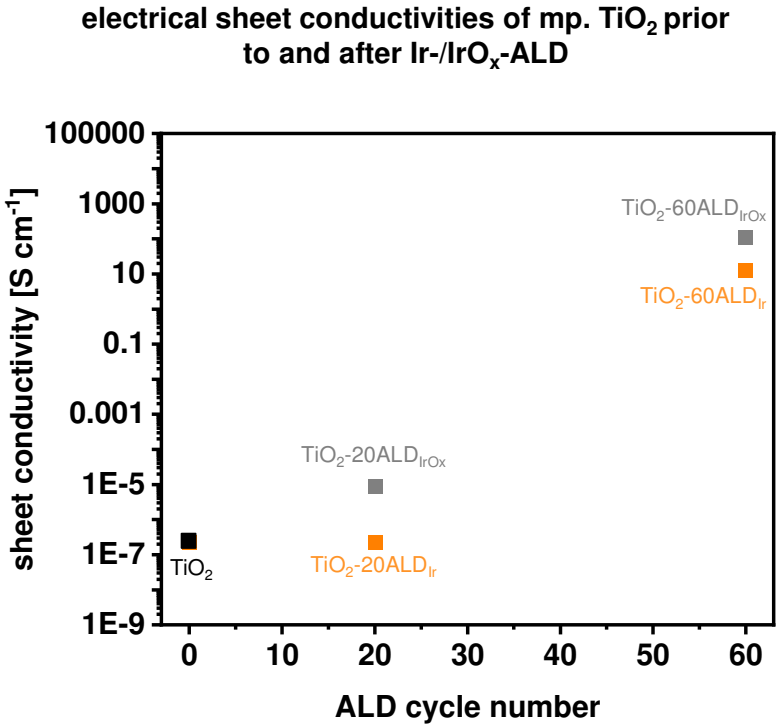

Figure S8. Electrical sheet conductivities assessed *via* impedance spectroscopy of mp. TiO_2 (black square) as well as TiO_2 supports modified *via* ALD at 160 °C (orange) and at 120 °C (grey). All investigated films were deposited on insulating glass substrates.

In accordance with our previous results[9,10] for sheet-thickness-normalized electrical conductivities, mp. TiO_2 films calcined at 475 °C show low conductivities of ~10^{-7} S cm^{-1}.

For low cycle numbers of ALD at 160 °C, *i.e.* 20 cycles, no change in conductivity can be observed. TiO_2-$20ALD_{Ir}$ shows a similar conductivity of ~10^{-7} S cm^{-1} as the bare mp. TiO_2 support. This can be explained by the deposition of nanoparticulate Ir species, rather than conformal surface layers (*cf.* **Figure 1** in the main part). Evidently, the overall sheet conductivity is dominated by the carrier matrix, *i.e.* the semiconducting TiO_2.[11]

For low cycle numbers of ALD at 120 °C, however, a rise in conductivity to ~10^{-5} S cm^{-1} is found, underlining the formation of an ultra-thin surface layer which coats the entire pore wall surface of the support. For a higher ALD cycle number, *i.e.* 60 cycles, a steep increase in sheet conductivities can be seen independent of the temperature during ALD. Accordingly, high loadings of well-conductive surface Ir species lead to a significant rise in film conductivity by

the formation of conductive surface electron pathways.[12,13] Schlicht *et al.*[11] reported similar observations regarding the formation of continuous conduction paths by high ALD cycle numbers for Ir deposited on TiO_2 nanotube arrays.

Section-IX: Cyclic voltammetry and base voltammetry of mp. $IrTiO_x$ prior to and after ALD at 120 °C

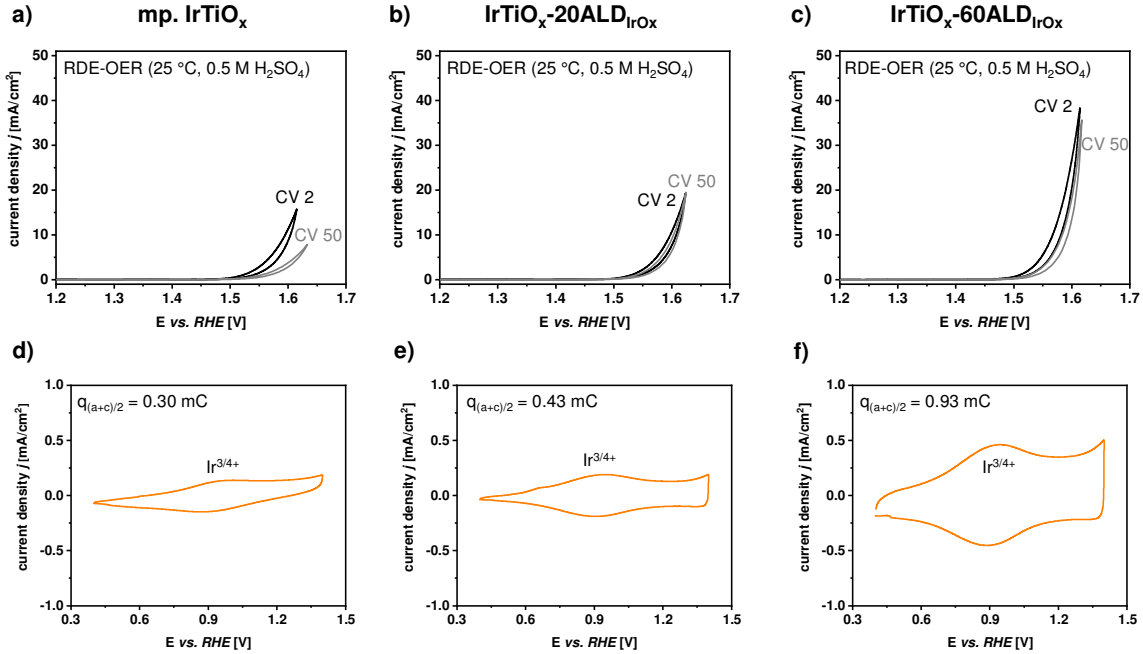

Figure S9. 2nd and 50th CVs from RDE-OER measurements of (a) mp. $IrTiO_x$, (b) $IrTiO_x$-$20ALD_{IrOx}$ and (c) $IrTiO_x$-$60ALD_{IrOx}$ in 0.5 M H_2SO_4 (N_2-sat.) at 25 °C and 1600 rpm rotation of the working electrode. The geometric current densities are plotted vs. potential (vs. RHE). (d) – (f) represent the CVs from base voltammetry at a lower potential for (d) mp. $IrTiO_x$, (e) $IrTiO_x$-$20ALD_{IrOx}$ and (f) $IrTiO_x$-$60ALD_{IrOx}$. $Ir^{3/4+}$ redox transitions at ~ 0.9 V_{RHE} are clearly visible in (d) – (e), which is in accordance with our previous results.

Figure S9 illustrates the results from electrochemical testings in a RDE setup using 0.5 M H_2SO_4 as a supporting electrolyte at 25 °C for mp. $IrTiO_x$ films prior to (**Figure S9a**) and after surface-modification with IrO_x species *via* low-temperature ALD at 120 °C (**Figure S9b-c**). The films show a similar average sheet thickness of ~ 100 nm, which remains essentially unaltered after ALD. For an increasing ALD cycle number, the amount of Ir loaded in the catalyst films rises and, concomitantly, the geometric current densities increase in the OER regime. In **Figure S9d-f**, the anodic and cathodic charge in a lower potential range are given (base voltammetry). Redox peaks of the $Ir^{3/4+}$ couple are clearly visible. For higher ALD cycle numbers, the average anodic and cathodic charge increases, which indicates an increasing number of accessible active metal centers in the films.

Section-X: Geometric current density – potential and corresponding Ir mass-normalized activity plots *via* cyclic voltammetry (RDE-OER) measurements in 0.5 M H_2SO_4

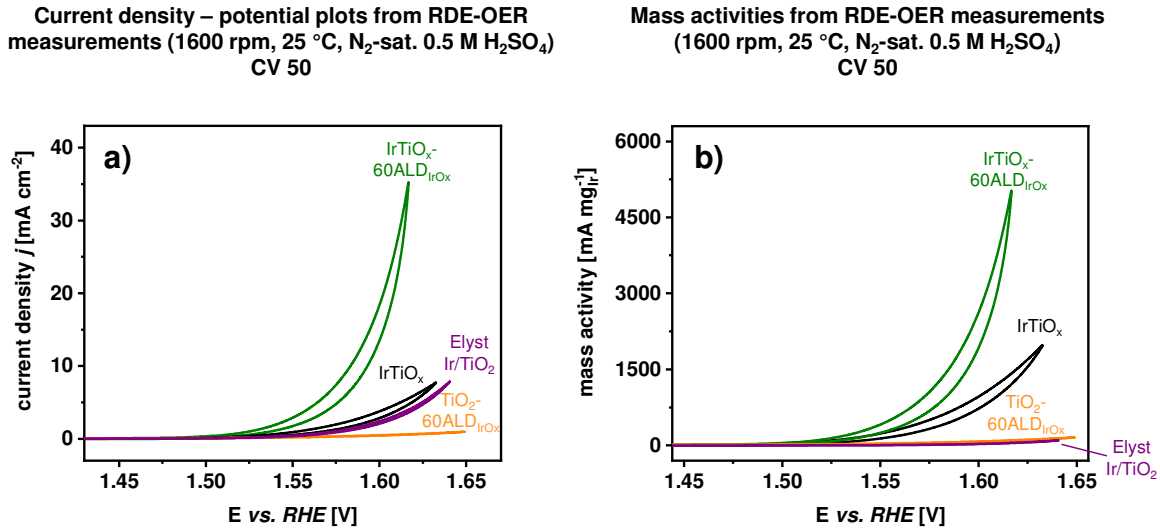

Figure S10. Current density vs. potential plots from RDE-OER measurements in 0.5 M H_2SO_4 (N_2-sat.) at 25 °C and 1600 rpm rotation. The geometric current densities are plotted vs. potential (vs. RHE) in (a). The corresponding potential-dependent Ir-mass-specific activities are given in (b). Selected catalysts are shown, *i.e.* $IrTiO_x$ (black), $IrTiO_x$-$60ALD_{IrOx}$ (dark green), TiO_2-$60ALD_{IrOx}$ (orange) and the commercial reference Elyst Ir/TiO_2 (purple).

Figure S10 shows the results from RDE-OER testings for selected catalyst systems. After normalization of the currents to the respective Ir loadings in the catalyst films (see **Figure S10b**), the significantly improved catalytic OER activity of the top-performing catalyst, $IrTiO_x$-$60ALD_{IrOx}$ (dark green curve), becomes evident. The commercial reference catalyst, Elyst Ir/TiO_2 (purple) shows the lowest mass activities in the investigated potential range.

Section-XI: Evaluation of Tafel slopes *via* RDE-OER in 0.5 M H_2SO_4

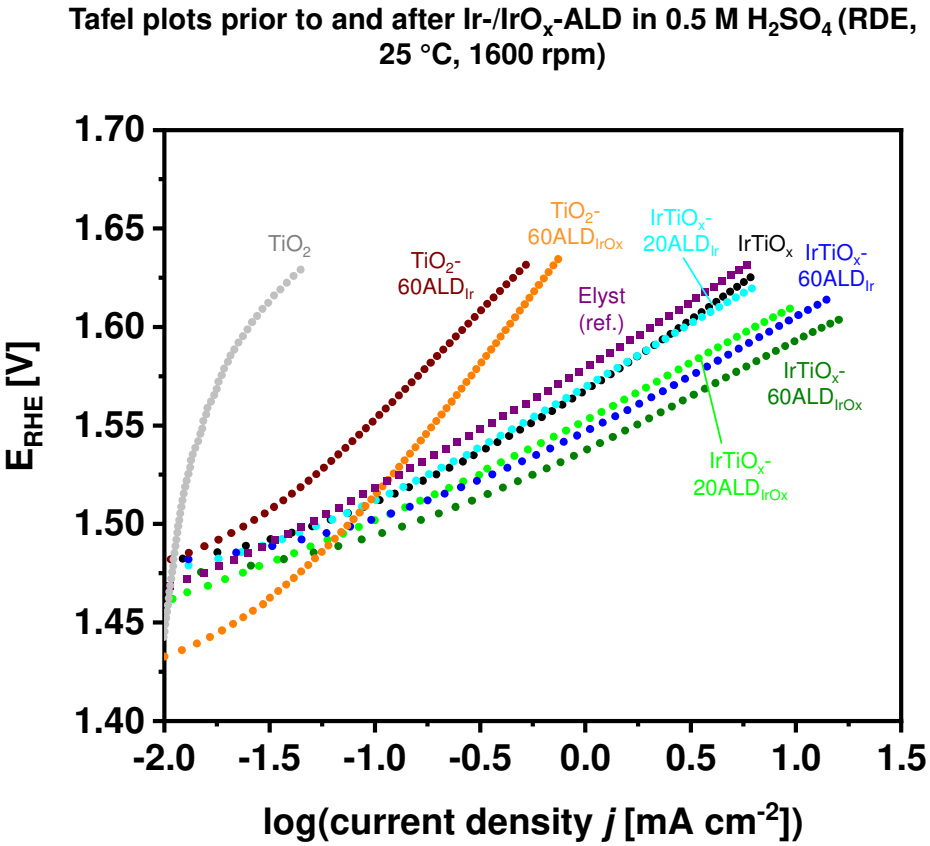

Figure S11. Tafel plots calculated from the 50th CV from RDE-OER measurements of all catalyst films listed in **Table 1** in the manuscript. The corresponding Tafel slopes were calculated in a potential range between 1.55 – 1.60 V_{RHE}.

Next, as a highly relevant indicator for the ongoing reaction kinetics, Tafel slopes of the electrocatalysts were derived from the corresponding CVs. In brief, significantly higher Tafel slopes were found for all surface-modified as well as unmodified films with TiO_2 as a support compared to $IrTiO_x$-supported catalysts. Regarding the latter, slightly smaller values were obtained after both ALD at 120 °C and at 160 °C, indicating faster reaction kinetics compared to the unmodified mp. $IrTiO_x$ support. This enhancement might be related to a higher absolute number of electrochemically accessible metal centers after surface-modification *via* ALD. In this context, ALD at 120 °C leads to the deposition of highly homogeneous IrO_x surface layers with low crystallinity and, thus, promotes OER kinetics as a result of the high intrinsic activity of Ir^{3+} species towards oxygen evolution. Yet, a sufficient electrical bulk conductivity is mandatory for high OER activities, which becomes evident upon comparison of TiO_2-

$60ALD_{IrOx}$ vs. $IrTiO_x$-$60ALD_{IrOx}$. With only 55 mV dec^{-1}, the latter shows the smallest Tafel slope (50^{th} CV, down-cycle), whereas with more than 100 mV dec^{-1}, the former suffers from sluggish reaction kinetics.

In accordance with previous investigations[10,14] regarding potential-dependent changes in the Tafel slopes of Ir-based OER catalysts, all Ir/IrO_x-modified films show a characteristic kink for higher potentials than ~1.50 – 1.55 V_{RHE}. The observed bend in the Tafel slope seems slightly more pronounced for IrO_x-modified catalysts *via* ALD at 120 °C. As nicely discussed by Nong *et al.*[14], this effect can be related to a variation in the coverage of surface holes (h^+) over potential.

Section XII: Impact of ALD on ECSA estimated from base voltammetry

It was shown that the parameters of the ALD process, primarily the temperature during deposition, affect the chemical nature of the Ir species distributed on the surface of the three-dimensional mesoporous network with interconnected porosity.

Base voltammetry in a lower potential range between 0.4 – 1.4 V_{RHE} reveals distinct differences for the average anodic and cathodic charge dependent on the structure and electrical properties of the support. Unmodified mp. TiO_2 shows only a negligible charge calculated from the mean value of the integrated cathodic and anodic scan of the *iR*-corrected CV curve (see **Figure S12b**, grey curve), whereas for mp. $IrTiO_x$ a higher charge $q_{(a+c)/2}$ with small peaks characteristic of redox features of accessible Ir surface sites can be found in the corresponding CV in **Figure S12a** (black curve). After ALD, the charge increases for both $IrTiO_x$-$60ALD_{Ir}$ and $IrTiO_x$-$60ALD_{IrOx}$, confirming their superior OER activities as a consequence of a higher number of accessible catalytically active centers.

In the case of TiO_2-supported catalysts, however, no characteristic $Ir^{3/4+}$ redox peaks can be found in the resulting CVs (see **Figure S12b**). Even though, after ALD, numerous surface Ir species are present, an insufficient bulk electrical conductivity seems to hamper relevant Faradaic currents. Hence, no redox peaks characteristic of active Ir sites can be found in the base voltammograms.

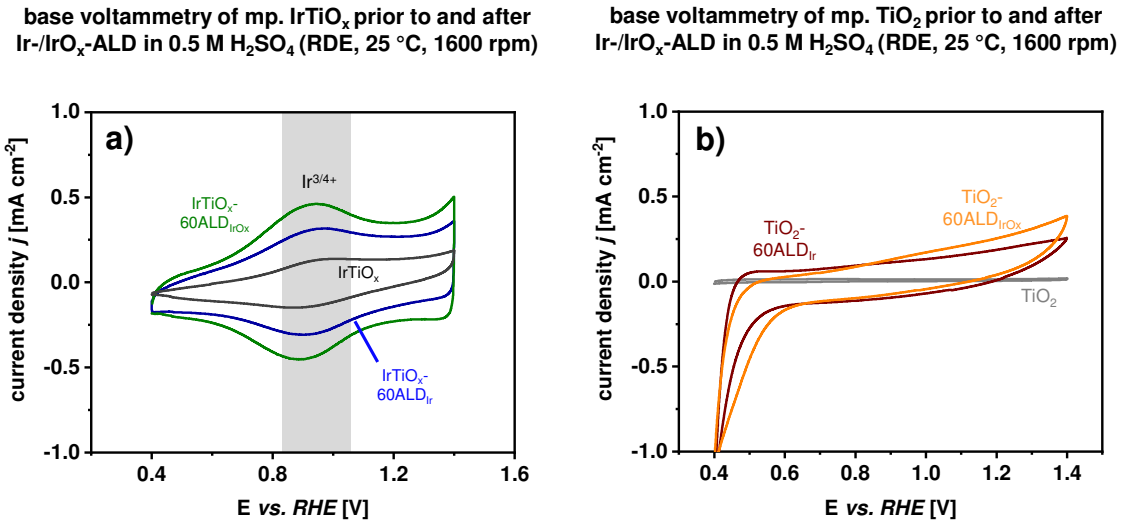

Figure S12. Base voltammetry measurements in a RDE-OER setup of (a) mp. $IrTiO_x$ (black) and (b) TiO_2 (grey) in 0.5 M H_2SO_4. The geometric current densities are plotted vs. potential (vs. RHE). In (a), CVs for $IrTiO_x$-$60ALD_{Ir}$ and $IrTiO_x$-$60ALD_{IrOx}$ are shown in dark blue and green, respectively. $Ir^{3/4+}$ redox transitions at ~ 0.9 V_{RHE} are clearly visible in (a). In (b), CVs for TiO_2-$60ALD_{Ir}$ and TiO_2-$60ALD_{IrOx}$ are illustrated in dark red and orange, respectively. No characteristic Ir redox peaks can be found in (b).

Section XIII: Chronopotentiometric stability tests of mp. $IrTiO_x$ prior to and after IrO_x-ALD

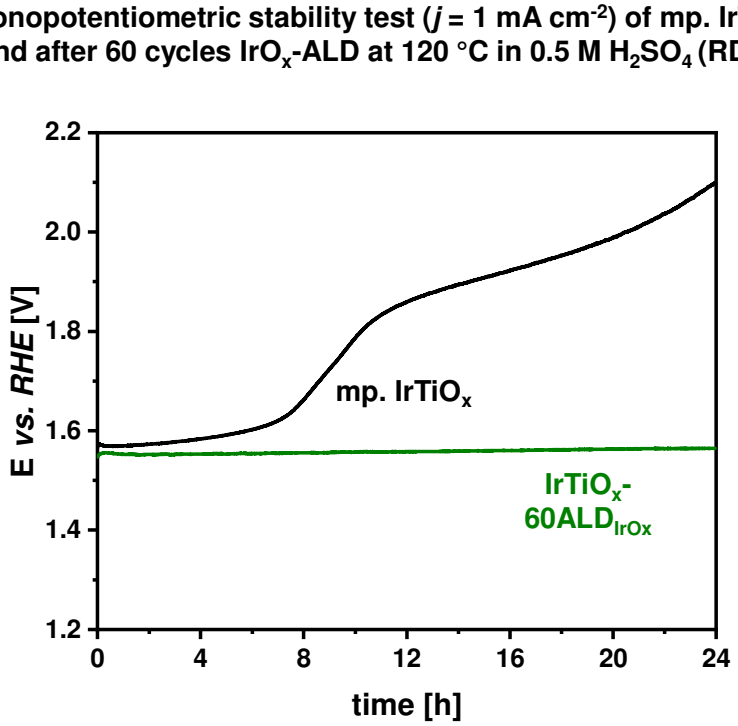

Figure S13. Chronopotentiometric stability tests in an RDE-OER setup of mp. $IrTiO_x$ (black) and $IrTiO_x$-$60ALD_{IrOx}$ (dark green) in 0.5 M H_2SO_4 at 25 °C. The potential (vs. RHE) is plotted over time in electrolyte and j = 1 mA cm^{-2}.

In order to investigate the influence of the ALD process at 120 °C on the electrochemical stability of the films, chronopotentiometry measurements were performed in 0.5 M H_2SO_4 at 25 °C in an RDE setup. As shown in the results in **Figure S13**, surface-modified films are more robust OER catalysts. Prior to ALD, the conductive $IrTiO_x$ reveals an insufficient long-term stability in acid. After approximately 8 hours, pronounced dissolution of the film and a concomitant loss of active sites into the surrounding liquid electrolyte can be observed until the end of the 24-hour stability test.

Contrarily, for the most active herein developed catalyst, $IrTiO_x$-$60ALD_{IrOx}$, a different picture is revealed. Accordingly, the introduction of conformal IrO_x surface layers *via* ALD successfully protects the underlying iridium titania in the mp. $IrTiO_x$ support from an ongoing dissolution under corrosive and oxidative conditions.

Our results serve as a proof-of-principle, highlighting the role of the ALD surface layer in enhancing the durability of the electrocatalyst, as evidenced by the results from static operation conditions on the RDE level. It has to be noted that recent literature[15,16] proposes accelerated degradation/stress tests on the MEA (membrane electrode assembly) level for a more realistic evaluation of catalyst stability. In this context, RDE testings are more appropriate for the determination of catalyst activity. This conclusion has been drawn based on systematic examinations on the influence of anionic species in the electrolytes used in RDE setups on the dissolution of different electrocatalysts.[17] In addition, the impact of accumulated gas bubbles (O_2) during RDE measurements has been thoroughly discussed. A partial shielding of active surface sites by evolving gas bubbles in the catalyst layer, which are not completely removed by the rotational forces, may contribute to a decrease in activity over time rather than degradation of the active material or phase(s).[16,18]

References

[1] V. Pfeifer, T. E. Jones, J. J. Velasco Vélez, C. Massué, R. Arrigo, D. Teschner, F. Girgsdies, M. Scherzer, M. T. Greiner, J. Allan, M. Hashagen, G. Weinberg, S. Piccinin, M. Hävecker, A. Knop-Gericke, R. Schlögl, *Surf. Interface Anal.* **2016**, *48*, 261–273.

[2] H. Y. Hall, P. M. A. Sherwood, *J. Chem. Soc. Faraday Trans. 1 Phys. Chem. Condens. Phases* **1984**, *80*, 135.

[3] E. Özer, Z. Pawolek, S. Kühl, H. Nong, B. Paul, S. Selve, C. Spöri, C. Bernitzky, P. Strasser, *Surfaces* **2018**, *1*, 151–164.

[4] S. J. Freakley, J. Ruiz-Esquius, D. J. Morgan, *Surf. Interface Anal.* **2017**, *49*, 794–799.

[5] F. Claudel, L. Dubau, G. Berthomé, L. Sola-Hernandez, C. Beauger, L. Piccolo, F. Maillard, *ACS Catal.* **2019**, *9*, 4688–4698.

[6] V. Pfeifer, T. E. Jones, J. J. Velasco Vélez, C. Massué, M. T. Greiner, R. Arrigo, D. Teschner, F. Girgsdies, M. Scherzer, J. Allan, M. Hashagen, G. Weinberg, S. Piccinin, M. Hävecker, A. Knop-Gericke, R. Schlögl, *Phys. Chem. Chem. Phys.* **2016**, *18*, 2292–2296.

[7] M. C. Biesinger, L. W. M. Lau, A. R. Gerson, R. S. C. Smart, *Appl. Surf. Sci.* **2010**, *257*, 887–898.

[8] Y. Fan, Y. Wu, G. Clavel, M. H. Raza, P. Amsalem, N. Koch, N. Pinna, *ACS Appl. Energy Mater.* **2018**, *1*, 4554–4563.

[9] D. Bernsmeier, M. Bernicke, R. Schmack, R. Sachse, B. Paul, A. Bergmann, P. Strasser, E. Ortel, R. Kraehnert, *ChemSusChem* **2018**, *11*, 2367–2374.

[10] M. Bernicke, D. Bernsmeier, B. Paul, R. Schmack, A. Bergmann, P. Strasser, E. Ortel, R. Kraehnert, *J. Catal.* **2019**, *376*, 209–218.

[11] S. Schlicht, P. Büttner, J. Bachmann, *ACS Appl. Energy Mater.* **2019**, *2*, 2344–2349.

[12] P. Schmitt, V. Beladiya, N. Felde, P. Paul, F. Otto, T. Fritz, A. Tünnermann, A. V. Szeghalmi, *Coatings* **2021**, *11*, 173.

[13] A. Szeghalmi, M. Arnold, A. Berger, N. Schammelt, K. Fuechsel, M. Knez, E. B. Kley, D. R. T. Zahn, A. Tuennermann, in (Eds.: M. Lequime, H.A. Macleod, D. Ristau), **2011**, p. 81680.

[14] H. N. Nong, L. J. Falling, A. Bergmann, M. Klingenhof, H. P. Tran, C. Spöri, R. Mom, J. Timoshenko, G. Zichittella, A. Knop-Gericke, S. Piccinin, J. Pérez-Ramírez, B. R. Cuenya, R. Schlögl, P. Strasser, D. Teschner, T. E. Jones, *Nature* **2020**, *587*, 408–413.

[15] C. Spöri, C. Brand, M. Kroschel, P. Strasser, *J. Electrochem. Soc.* **2021**, *168*, 034508.

[16] M. Bernt, A. Hartig-Weiß, M. F. Tovini, H. A. El-Sayed, C. Schramm, J. Schröter, C. Gebauer, H. A. Gasteiger, *Chemie Ing. Tech.* **2020**, *92*, 31–39.

[17] C. Van Pham, D. Escalera-López, K. Mayrhofer, S. Cherevko, S. Thiele, *Adv. Energy Mater.* **2021**, *11*, 2101998.

[18] H. A. El-Sayed, A. Weiß, L. F. Olbrich, G. P. Putro, H. A. Gasteiger, *J. Electrochem. Soc.* **2019**, *166*, F458–F464.